Phase-field-based calculations of the disregistry fields of static extended dislocations in FCC metals

Shuozhi Xu[a], Jaber R. Mianroodi[b,c], Abigail Hunter[d], Irene J. Beyerlein[a,e] and Bob Svendsen[b,c]

[a]California NanoSystems Institute, University of California, Santa Barbara, Santa Barbara, CA 93106-6105, USA; [b]Microstructure Physics and Alloy Design, Max-Planck-Institut für Eisenforschung GmbH, Düsseldorf, D-40237, Germany; [c]Material Mechanics, RWTH Aachen, Aachen, D-54062, Germany; [d]X Computational Physics Division, Los Alamos National Laboratory, Los Alamos, NM 87544, USA; [e]Department of Mechanical Engineering, Materials Department, University of California, Santa Barbara, Santa Barbara, CA 93106, USA

ARTICLE HISTORY
Compiled July 24, 2019

ABSTRACT
In the continuum context, the displacements of atoms induced by a dislocation can be approximated by a continuum disregistry field. In this work, two phase-field (PF)-based approaches and their variants are employed to calculate the disregistry fields of static, extended dislocations of pure edge and pure screw character in two face-centered cubic metals: Au and Al, which have distinct stable stacking fault energy and elastic anisotropy. A new truncated Fourier series form is developed to approximate the generalized stacking fault energy (GSFE) surface, which shows significant improvement over the previously employed Fourier series form. By measuring the intrinsic stacking fault (ISF) width and partial dislocation core size in different ways, the PF-based disregistry fields are quantitatively compared against those predicted by molecular statics. In particular, two new measures for the ISF widths are proposed and shown to overcome drawbacks of the more commonly used standards in the literature. Our calculations also show that continuum formulation of the elastic energy and the GSFE for a homogeneous surface can successfully characterize the core structure. Last, our comparisons highlight the significance of including the gradient energy in the free energy formulation when an accurate description of the dislocation core structure is desired.

KEYWORDS
Phase field; molecular statics; extended dislocation; intrinsic stacking fault

1. Introduction

Plastic deformation of crystalline materials, e.g., metals, alloys, semiconductors, ceramics, is controlled by the motion of dislocations [1]. The atomic structures of dislocation cores naturally depend on crystal arrangement of the atoms [2]. For example, in a face-centered cubic (FCC) lattice, a perfect $(a_0/2)\langle 110\rangle$ dislocation with a_0 being

CONTACT Shuozhi Xu. Email: shuozhixu@ucsb.edu

the lattice constant, is usually split into two Shockley partial dislocations

$$\frac{a_0}{2}\langle 110\rangle \longrightarrow \frac{a_0}{6}\langle 211\rangle + \frac{a_0}{6}\langle 121\rangle, \tag{1}$$

as a result of the unique energy landscape in FCC metals [3]. Because $(a_0/6)\langle 211\rangle$ is not a lattice translation vector, an intrinsic stacking fault (ISF) consisting of atoms in hexagonal close-packed (HCP) local structure is left behind as the first partial dislocation passes [4]. The atomic structure associated with the ISF is restored to that in a perfect lattice following the glide of the second partial dislocation. Therefore, a perfect dislocation in FCC metals is usually "extended", consisting of two partial dislocations bounding, and separated by, an ISF. These extended dislocations distinguish the plasticity of FCC metals from that in many other crystals and the extent of the stacking fault plays an important role in processes such as structural transformation, twinning, dislocation network formation [5, 6], dislocation reactions [7], and cross slip [8].

While atomistic simulations are desirable in modeling dislocations, they are limited to nano/submicron length scale even with dedicated high-performance computing resources [9, 10]. To understand plastic deformation of bulk materials, mesoscopic approaches are desirable, pointing to the need of mesoscale modeling of dislocation core structures which are building blocks for more complicated dislocation-mediated problems [11, 12]. From a computational perspective, it is challenging to model detailed and heterogeneous atomic-scale morphology of an extended dislocation since it cannot be treated as a sharp, homogeneous boundary between a slipped and an unslipped region in a lattice.

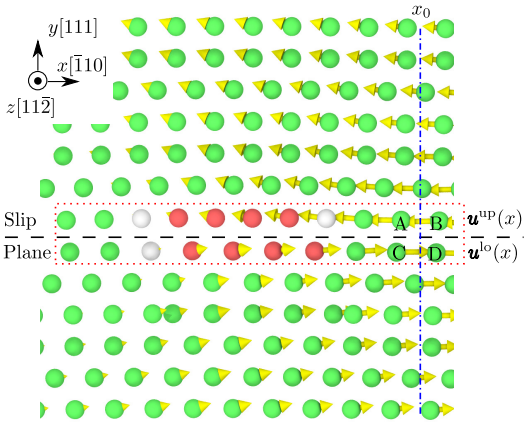

Figure 1. MS simulation results for the dissociation of an straight edge dislocation in Al. Atoms are colored by adaptive common neighbor analysis (a-CNA) [13]: green, red, and white correspond to FCC, HCP, and disordered local lattice structures, respectively. Each yellow arrow is the displacement vector of the associated atom with respect to its dislocation-free perfect lattice site. The blue dash-dotted vertical line is the position of x_0; the black dashed horizontal line shows the slip plane; the two layers of atoms immediately above and below the slip plane are within a red dotted box.

Fundamentally, the dislocation structure can be described by the displacements of discrete atoms with respect to their dislocation-free perfect lattice sites, as visualized by the yellow arrows in Fig. 1. In the continuum context, the discrete atomic displacements are instantiated by a continuum disregistry field $\boldsymbol{\zeta}(x)$ along the x direction, which, for any continuum point x_0, is

$$\boldsymbol{\zeta}(x_0) = \boldsymbol{u}^{\mathrm{up}}(x_0) - \boldsymbol{u}^{\mathrm{lo}}(x_0) \tag{2}$$

where $\boldsymbol{u}^{\mathrm{up}}(x_0)$ and $\boldsymbol{u}^{\mathrm{lo}}(x_0)$ are the continuum displacements at x_0 immediately above and below the slip plane, respectively. In Fig. 1, x_0 is located between atoms A and B in the upper plane and atoms C and D in the lower plane. Take the upper plane as an example, the displacement at x_0 can be linearly interpolated between those of atoms A and B ($\boldsymbol{u}^{\mathrm{A}}$ and $\boldsymbol{u}^{\mathrm{B}}$), i.e.,

$$\boldsymbol{u}^{\mathrm{up}}(x_0) = \boldsymbol{u}^{\mathrm{A}} + \frac{\boldsymbol{u}^{\mathrm{B}} - \boldsymbol{u}^{\mathrm{A}}}{x^{\mathrm{B}} - x^{\mathrm{A}}}(x_0 - x^{\mathrm{A}}) \tag{3}$$

where x^{A} and x^{B} are the x-coordinates of atoms A and B, respectively. The process to calculate $\boldsymbol{u}^{\mathrm{lo}}(x_0)$ is similar. Note that at any point x, the vector $\boldsymbol{\zeta}(x)$ can point to any direction, i.e., the disregistry field is inherently 3D. However, the component along the y direction is usually not considered in continuum simulations [14].

Eqs. 2 and 3 relate the discrete atomic displacements with a continuum disregistry field, making it possible for continuum methods, e.g., the generalized Peierls-Nabarro (GPN) model [15] and the phase-field (PF)-based methods [16, 17], to quantify the dislocation core structures in a manner consistent with atomistic simulations. GPN- and PF-based methods have been adapted to mechanics problems and more specifically for determining the core structures of dislocations [18, 19]. These methods minimize an energy functional at every point in the system and the order parameters are usually chosen to identify a slipped phase and unslipped phase. Furthermore, PF framework can be applied to the complex systems for which no reliable interatomic potential is available. The input parameters of PF model can be obtained from *ab initio* and/or experimental sources in such cases. In addition, the time scale limitation of full atomistic simulation prevents investigating diffusion-coupled phenomena. For example, the PF model can be used to couple displacive-diffusional dislocation models in complex materials, such as Ni-based superalloys [20]. Consequently, the PF method has the advantage of simulating the low energy state of a dislocation core, including the ISF width and two bounding partials.

While using the same basic PF framework, different variants of PF dislocation models have evolved over the years due to optional modeling choices. In this work, we examine the capabilities of different PF-based dislocation model variants by comparing the calculated disregistry profiles to molecular statics (MS) calculations. We choose two models, atomistic phase-field microelasticity (APFM) [17] and phase-field dislocation dynamics (PFDD) [16], which represent diverse modeling choices and thus find commonalities with others PF-based dislocation models in the literature. Note that in the special case of a straight dislocation, the PFDD model was found to be equivalent to the GPN model [21]. To ensure that the findings apply to a wide range of FCC materials, two metals, Au and Al, are selected since they have distinctly different stable SFE and elastic anisotropy. Once the disregistry fields are obtained, different methods are adopted to determine the ISF widths and Shockley partial dislocation core sizes.

In this paper, 3D Euclidean vectors are represented by lower-case bold italic characters $\boldsymbol{a}, \boldsymbol{b}, \ldots$ In particular, let $\boldsymbol{i}_1, \boldsymbol{i}_2, \boldsymbol{i}_3$ represent the Cartesian basis vectors. Second-order tensors are represented by upper-case bold italic characters $\boldsymbol{A}, \boldsymbol{B}, \ldots$ Third- and fourth-order Euclidean tensors $\boldsymbol{\mathsf{A}}, \boldsymbol{\mathsf{B}}, \ldots$ are denoted by upper-case slanted sans-serif characters. The transpose $\boldsymbol{A}^{\mathrm{T}}$ of $\boldsymbol{A}$ is defined by $\boldsymbol{A}^{\mathrm{T}}\boldsymbol{b} \cdot \boldsymbol{c} = \boldsymbol{b} \cdot \boldsymbol{A}\boldsymbol{c}$. Additional notation will be introduced as needed in what follows.

2. A brief summary of PF-based modeling of dislocations

Following Mianroodi et al. [21], let $\boldsymbol{u}$ represent the displacement field, $\boldsymbol{H} = \nabla \boldsymbol{u}$ the distortion field, $\boldsymbol{E} = (\boldsymbol{H} + \boldsymbol{H}^{\mathrm{T}})/2$ the strain field, and $\boldsymbol{\phi} = (\phi_1, \ldots, \phi_n)$ a set of n order parameters, with ϕ_α ranging between 0 and 1 for one perfect dislocation.

In the absence of an externally applied stress, the free energy density ψ takes the form

$$\psi(\boldsymbol{E}, \boldsymbol{\phi}, \nabla\boldsymbol{\phi}) = \psi_{\mathrm{ela}}(\boldsymbol{E}, \boldsymbol{\phi}) + \psi_{\mathrm{gsf}}(\boldsymbol{\phi}) + \psi_{\mathrm{gra}}(\nabla\boldsymbol{\phi}). \tag{4}$$

The elastic part is given by the Khachaturyan-Shalatov microelastic relation [18, 22, 23], i.e.,

$$\psi_{\mathrm{ela}}(\boldsymbol{E}, \boldsymbol{\phi}) = \frac{1}{2}(\boldsymbol{E} - \boldsymbol{E}_{\mathrm{R}}(\boldsymbol{\phi})) \cdot \boldsymbol{C}_{\mathrm{E}}(\boldsymbol{E} - \boldsymbol{E}_{\mathrm{R}}(\boldsymbol{\phi})) \tag{5}$$

where $\boldsymbol{C}_{\mathrm{E}}$ is the elastic stiffness and $\boldsymbol{E}_{\mathrm{R}} = (\boldsymbol{H}_{\mathrm{R}} + \boldsymbol{H}_{\mathrm{R}}^{\mathrm{T}})/2$ is the residual strain. For dislocation slip, the residual distortion, $\boldsymbol{H}_{\mathrm{R}}$, takes the form [22, 24, 25]

$$\boldsymbol{H}_{\mathrm{R}}(\boldsymbol{\phi}) = \sum_{\alpha=1}^{n} \eta_\alpha(\phi_\alpha) \boldsymbol{s}_\alpha \otimes \boldsymbol{n}_\alpha \tag{6}$$

where n is the total number of order parameters, $\boldsymbol{n}_\alpha$ is the slip plane unit normal, η_α the amount of shear distortion, and $\boldsymbol{s}_\alpha$ the slip direction, of the αth order parameter. Note that $\boldsymbol{E}$ is associated with $\boldsymbol{E}_{\mathrm{R}}$, and hence $\boldsymbol{H}_{\mathrm{R}}$ and $\boldsymbol{\phi}$, following the stress equilibrium [19].

The generalized SF energy (GSFE) density, $\psi_{\mathrm{gsf}}(\boldsymbol{\phi})$, represents the energy density associated with the ISF (the red atoms in Fig. 1). It is related to the GSFE surface γ_{gsf} via a scaling factor l_{gsf}, i.e.,

$$\psi_{\mathrm{gsf}}(\boldsymbol{\phi}) = \frac{\gamma_{\mathrm{gsf}}(\boldsymbol{\phi})}{l_{\mathrm{gsf}}} \tag{7}$$

The gradient energy density, ψ_{gra}, represents the density of energy storage in the Shockley partial dislocation cores (the white atoms in Fig. 1). For dislocation glide with planar cores in a single crystal, ψ_{gra} is given by [26]

$$\psi_{\mathrm{gra}}(\nabla\boldsymbol{\phi}) = \eta_{\mathrm{g0}} \left| \operatorname{curl} \boldsymbol{H}_{\mathrm{R}} \right|^2 = \eta_{\mathrm{g0}} \sum_{\alpha,\beta=1}^{n} \nabla\phi_\alpha \cdot \boldsymbol{N}_{\alpha\beta} \nabla\phi_\beta \tag{8}$$

where

$$\boldsymbol{N}_{\alpha\beta} = \frac{\boldsymbol{b}_\alpha \cdot \boldsymbol{b}_\beta}{d_{111}^2} \left[(\boldsymbol{n}_\alpha \cdot \boldsymbol{n}_\beta)\boldsymbol{I} - \boldsymbol{n}_\beta \otimes \boldsymbol{n}_\alpha \right] \tag{9}$$

where $\boldsymbol{I}$ is the second-order identity matrix, $\boldsymbol{b}_\alpha$ and $\boldsymbol{b}_\beta$ are the slip vectors, which are not necessarily the Burgers vector, $d_{111} = a_0/\sqrt{3}$ is the distance between two adjacent $\{111\}$ plane in an FCC lattice, and $\boldsymbol{N}_{\alpha\beta}$ is a unitless second-order projection tensor

which projects $\nabla\boldsymbol{\phi}$ onto the slip planes. The scaling factor η_{g0}, which has units of energy per unit length, is informed by MS simulations following [17]

$$\eta_{\mathrm{g0}} = \frac{g_0 l_0}{\alpha_{\mathrm{g0}}} \tag{10}$$

where α_{g0}, g_0, and l_0 are fit to MS-based extended dislocation configuration. We remark that introducing the MS-informed scaling factor yields a gradient energy density that better represents the contribution from the Shockley partial dislocation cores. In particular, l_0 is the Shockley partial dislocation core size and will be further discussed in Section 5.3. Note that with respect to our earlier publications [17, 21] in which κ was used for two scaling factors, the following relation holds:

$$\alpha_{\mathrm{g0}} = \kappa_{\mathrm{G0}}\kappa_{\mathrm{H0}} \tag{11}$$

Once the free energy density ψ is calculated, the time-dependent Ginzburg-Landau (TDGL) equation is employed to recursively minimize ψ with respect to each ϕ_α, i.e.,

$$\dot{\phi}_\alpha = -m_0 \delta_{\phi_\alpha} \psi \tag{12}$$

where the superposed dot denotes the time derivative, and the mobility m_0 is assumed a non-negative constant for all order parameters for simplicity and to ensure non-negative dissipation and gradient flow of the system toward thermodynamic equilibrium.

3. Formulation and parameterization in APFM and PFDD

Table 1. A summary of the differences among the four PF-based methods that are employed in this work. n is the total number of order parameters for all possible slip systems; h is the uniform grid spacing in a structured grid; $\boldsymbol{C}_{\mathrm{E}}$ is the elastic stiffness tensor; η_α is the amount of shear of the αth order parameter; ψ_{gra} is the gradient energy density; γ_{gsf} is the GSFE surface, and l_{gsf} is the factor between the GSFE density ψ_{gsf} and γ_{gsf} in Eq. 7.

	n	h	$\boldsymbol{C}_{\mathrm{E}}$	η_α	ψ_{gra}	γ_{gsf}	l_{gsf}	TDGL
APFM	8	$a_0/\sqrt{3}$	anisotropic	$b^{\mathrm{A}}_\alpha \phi^{\mathrm{A}}_\alpha / d_{111}$	Yes	Look-up table form	d_{111}	Eq. 13
$\mathrm{APFM_{ng}}$	8	$a_0/\sqrt{3}$	anisotropic	$b^{\mathrm{A}}_\alpha \phi^{\mathrm{A}}_\alpha / d_{111}$	No	Look-up table form	d_{111}	Eq. 14
PFDD	12	$a_0/\sqrt{2}$	isotropic	$b^{\mathrm{P}}_\alpha \delta_\alpha \phi^{\mathrm{P}}_\alpha$	No	Look-up table form	b^{P}	Eq. 14
$\mathrm{PFDD_{fs}}$	12	$a_0/\sqrt{2}$	isotropic	$b^{\mathrm{P}}_\alpha \delta_\alpha \phi^{\mathrm{P}}_\alpha$	No	Eq. 26	b^{P}	Eq. 14

APFM and PFDD differ in many ways in terms of formulation and parametrization, and we are motivated to understand the impact of these choices on the predicted disregistry fields of the same dislocation. One major difference between the two methods is that in APFM, Eq. 4 is fully employed, while in PFDD, the effect of the order parameter gradient, $\nabla\boldsymbol{\phi}$, is not considered, and so ψ_{gra} is neglected. To assess the influence of this difference, ψ_{gra} is intentionally omitted in some APFM calculations, and the corresponding results are termed "$\mathrm{APFM_{ng}}$"; otherwise, the APFM-based results are simply referred to as "APFM". Another difference concerns the calculation of γ_{gsf} in Eq. 7. Based on *ab initio* or atomistic GSFE data, γ_{gsf} is usually represented in look-up table form [17] or in 2D truncated Fourier series form [27]. While both forms are implemented into PFDD, only the look-up table form is employed in

APFM. To consider this difference, the PFDD-based results based on the look-up table and Fourier series forms are termed "PFDD" and "PFDD$_{\text{fs}}$", respectively. As a result, this paper effectively adopts four variants of PF-based approaches: APFM, APFM$_{\text{ng}}$, PFDD, PFDD$_{\text{fs}}$. It follows that the TDGL equation becomes

$$\dot{\phi}_\alpha = m_0 \left[\nabla \cdot \partial_{\nabla\phi_\alpha}\psi - \partial_{\phi_\alpha}\psi\right] \tag{13}$$

in APFM and

$$\dot{\phi}_\alpha = -m_0 \partial_{\phi_\alpha}\psi \tag{14}$$

in APFM$_{\text{ng}}$, PFDD, and PFDD$_{\text{fs}}$. In all four methods, the embedded-atom method (EAM) potentials for Au [28] and Al [29] are employed to calculate certain parameters. All differences among these methods are summarized in Tab. 1; more details are provided in the remainder of this section.

3.1. *Order parameter ϕ*

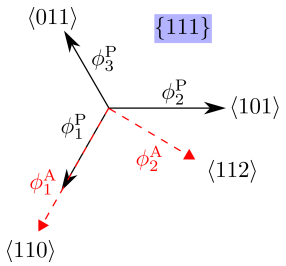

Figure 2. An illustration of the two order parameters (ϕ_1^{A}, ϕ_2^{A}) in APFM and APFM$_{\text{ng}}$, and the three (ϕ_1^{P}, ϕ_2^{P}, ϕ_3^{P}) in PFDD and PFDD$_{\text{fs}}$.

Let $b_\alpha = |\boldsymbol{b}_\alpha|$ be the magnitude of $\boldsymbol{b}_\alpha$. In APFM and APFM$_{\text{ng}}$, two order parameters, one along $\langle 110\rangle$, and the other along $\langle 112\rangle$, are employed on each $\{111\}$ plane [17]. Accordingly, $b_1 = \sqrt{2}a_0/2$ and $b_2 = \sqrt{6}a_0/2$. Given that there are four equivalent $\{111\}$ planes in an FCC lattice, the total number of order parameters $n = 8$ in the APFM-based variants. In PFDD and PFDD$_{\text{fs}}$, three order parameters, each corresponding to one of the $\langle 110\rangle$ directions on the slip plane, are used per $\{111\}$ plane, and so $b_\alpha = \sqrt{2}a_0/2$ for all order parameters and $n = 12$ to account for all possible slip systems. On one $\{111\}$ plane, the two sets of order parameters can be related following two steps: first, due to the crystallographic symmetry, any ϕ_α^{P} with α being 1, 2, or 3 can be assumed along ϕ_1^{A}; second, if ϕ_2^{A} is in the clockwise/counterclockwise direction of ϕ_1^{A}, the remaining two ϕ_α^{P} must also be sequentially in the clockwise/counterclockwise direction of the first ϕ_α^{P}. In this work, as illustrated in Fig. 2, the relations are

$$\phi_1^{\text{A}} = \frac{b^{\text{P}}}{b_1^{\text{A}}}(\phi_1^{\text{P}} - \phi_2^{\text{P}}\cos 60^\circ - \phi_3^{\text{P}}\cos 60^\circ) = \phi_1^{\text{P}} - \frac{1}{2}(\phi_2^{\text{P}} + \phi_3^{\text{P}}) \tag{15}$$

$$\phi_2^{\text{A}} = \frac{b^{\text{P}}}{b_2^{\text{A}}}(\phi_2^{\text{P}}\sin 60^\circ - \phi_3^{\text{P}}\sin 60^\circ) = \frac{1}{2}(\phi_2^{\text{P}} - \phi_3^{\text{P}}) \tag{16}$$

where superscripts A and P stand for APFM-based and PFDD-based variants, respectively. In what follows, we let $b^{\text{P}} = \sqrt{2}a_0/2$.

3.2. *Elastic energy density* ψ_{ela}

Table 2. Lattice parameter a_0 (in units of Å) and elastic constants C_{11}, C_{12}, C_{44} (in units of GPa) are calculated from the EAM potentials for Au [28] and Al [29].

	a_0	C_{11}	C_{12}	C_{44}
Au	4.08	201.65	169.53	45.97
Al	4.05	113.80	61.55	31.60

In Eq. 6, $\eta_\alpha(\phi_\alpha^{\text{A}}) = b_\alpha^{\text{A}}\phi_\alpha^{\text{A}}/d_{111}$ in APFM-based variants, and $\eta_\alpha(\phi_\alpha^{\text{P}}) = b_\alpha^{\text{P}}\delta_\alpha\phi_\alpha^{\text{P}}$ in PFDD-based variants, with δ_α being the glide-plane Dirac measure. In practice, δ_α equals the reciprocal of the grid spacing along the $\boldsymbol{n}_\alpha$ direction. In all methods, lattice parameter a_0 is needed to determine b_α. In Eq. 5, the elastic stiffness tensor $\boldsymbol{C}_{\text{E}}$ — for cubic systems, the three elastic constants C_{11}, C_{12}, C_{44} — are required. The four parameters are summarized in Tab. 2. In APFM-based variants, the anisotropic elastic stiffness tensor $\boldsymbol{C}_{\text{E}}$ is built directly from the three elastic constants. In PFDD-based variants, the medium is assumed elastically isotropic, and so two independent elastic parameters — Lamé constants μ and λ — are calculated by Voigt average [30], i.e.,

$$\mu = \frac{3C_{44} + C_{11} - C_{12}}{5} \tag{17}$$

$$\lambda = \frac{4C_{12} + C_{11} - 2C_{44}}{5} \tag{18}$$

which are then used to form $\boldsymbol{C}_{\text{E}}$.

3.3. *Generalized stacking fault energy density* ψ_{gsf}

In Eq. 7, $l_{\text{gsf}} = d_{111}$ and b^{P} in APFM-based and PFDD-based variants, respectively. In terms of the determination of the GSFE surface, γ_{gsf}, the first way is the look-up table form. To this end, a simulation box containing 2700 atoms that initially sit at their perfect lattice sites is subject to 199 and 598 displacement steps in the $[\bar{1}10]$ and $[\bar{1}\bar{1}2]$ directions, respectively. Following each displacement, the system is relaxed using a conjugate gradient algorithm with the atoms allowed to move along the (111) slip plane normal direction. For each displacement set $[\phi_{\bar{1}10}, \phi_{\bar{1}\bar{1}2}]$, the excess energy per unit ISF area relative to the ideal FCC lattice is taken as γ_{gsf}. To calculate the GSFE part of $\partial_{\phi_\alpha}\psi$ in Eqs. 13 and 14, i.e., $\partial_{\phi_\alpha}\psi_{\text{gsf}} = \partial_{\phi_\alpha}\gamma_{\text{gsf}}/l_{\text{gsf}}$, for each $[\phi_{\bar{1}10}, \phi_{\bar{1}\bar{1}2}]$, we take advantage of the following Fourier transform property,

$$\partial_{\phi_\alpha}\gamma_{\text{gsf}}(\phi_{\bar{1}10}, \phi_{\bar{1}\bar{1}2}) = \mathbb{R}\left(\mathcal{F}^{-1}\left[q_\alpha\hat{\gamma}_{\text{gsf}}(k_{\bar{1}10}, k_{\bar{1}\bar{1}2})\right]\right) \tag{19}$$

where the superposed hat denotes a 2D discrete Fourier transform from physical space $(\phi_{\bar{1}10}, \phi_{\bar{1}\bar{1}2})$ to Fourier space $(k_{\bar{1}10}, k_{\bar{1}\bar{1}2})$, $\mathcal{F}^{-1}$ conducts the inverse 2D discrete Fourier transform, and q_α is given by [31]

$$q_\alpha = iN_\alpha \sin(k_\alpha/N_\alpha) \tag{20}$$

where $N_\alpha = 199$ and 598 are the numbers of discrete GSFE data in the $[\bar{1}10]$ and $[\bar{1}\bar{1}2]$ directions, respectively, and the wave numbers k_α are

$$k_\alpha = 2\pi \left\{ 0, 1, ..., \left\lfloor \frac{N_\alpha}{2} \right\rfloor, \left\lceil \frac{1 - N_\alpha}{2} \right\rceil ..., -1 \right\} \tag{21}$$

In the meantime, a given set of ϕ_1^{A} and ϕ_2^{A} — either directly obtained in APFM and $\mathrm{APFM_{ng}}$ or transformed from $\boldsymbol{\phi}^{\mathrm{P}}$ using Eqs. 15 and 16 in PFDD and $\mathrm{PFDD_{fs}}$ — should be mapped into [0,1], by

$$\phi_\alpha^{\mathrm{A}} = \phi_\alpha^{\mathrm{A}} - \left\lfloor \phi_\alpha^{\mathrm{A}} \right\rfloor \tag{22}$$

if $\phi_\alpha^{\mathrm{A}} < 0$ or $\phi_\alpha^{\mathrm{A}} > 1$, which may occur in the presence of dislocations with negative signs or multiple dislocations in the same slip plane. This mapping is needed because the look-up table form only considers one period within the GSFE landscape, since it reflects atomic periodicity of the crystal. Note that the mapping is only carried out locally in calculating ψ_{gsf}, but not ψ_{ela} or ψ_{gra}. For the Fourier series-based γ_{gsf}, however, this mapping is not necessary since its periodicity is guaranteed by the trigonometric functions f_i (Eq. 26).

Once the 2D discrete $\partial_{\phi_\alpha}\gamma_{\mathrm{gsf}}(\phi_{\bar{1}10}, \phi_{\bar{1}\bar{1}2})$ surface is obtained, a bilinear interpolation is conducted for each order parameter α to calculate $\partial_{\phi_\alpha^{\mathrm{A}}}\gamma_{\mathrm{gsf}}(\phi_1^{\mathrm{A}}, \phi_2^{\mathrm{A}})$ in a look-up-table fashion. In APFM and $\mathrm{APFM_{ng}}$, the interpolated $\partial_{\phi_\alpha^{\mathrm{A}}}\gamma_{\mathrm{gsf}}$ is used directly in Eq. 13. However, in PFDD, it is $\partial_{\phi_\alpha^{\mathrm{P}}}\gamma_{\mathrm{gsf}}$ that is used in Eq. 14. Thus, with the help of Eqs. 15 and 16, adopting the chain rule yields

$$\partial_{\phi_1^{\mathrm{P}}}\gamma_{\mathrm{gsf}} = \partial_{\phi_1^{\mathrm{A}}}\gamma_{\mathrm{gsf}} \cdot \partial_{\phi_1^{\mathrm{P}}}\phi_1^{\mathrm{A}} + \partial_{\phi_2^{\mathrm{A}}}\gamma_{\mathrm{gsf}} \cdot \partial_{\phi_1^{\mathrm{P}}}\phi_2^{\mathrm{A}} = \partial_{\phi_1^{\mathrm{A}}}\gamma_{\mathrm{gsf}} \tag{23}$$

$$\partial_{\phi_2^{\mathrm{P}}}\gamma_{\mathrm{gsf}} = \partial_{\phi_1^{\mathrm{A}}}\gamma_{\mathrm{gsf}} \cdot \partial_{\phi_2^{\mathrm{P}}}\phi_1^{\mathrm{A}} + \partial_{\phi_2^{\mathrm{A}}}\gamma_{\mathrm{gsf}} \cdot \partial_{\phi_2^{\mathrm{P}}}\phi_2^{\mathrm{A}} = -\frac{1}{2}\partial_{\phi_1^{\mathrm{A}}}\gamma_{\mathrm{gsf}} + \frac{1}{2}\partial_{\phi_2^{\mathrm{A}}}\gamma_{\mathrm{gsf}} \tag{24}$$

$$\partial_{\phi_3^{\mathrm{P}}}\gamma_{\mathrm{gsf}} = \partial_{\phi_1^{\mathrm{A}}}\gamma_{\mathrm{gsf}} \cdot \partial_{\phi_3^{\mathrm{P}}}\phi_1^{\mathrm{A}} + \partial_{\phi_2^{\mathrm{A}}}\gamma_{\mathrm{gsf}} \cdot \partial_{\phi_3^{\mathrm{P}}}\phi_2^{\mathrm{A}} = -\frac{1}{2}\partial_{\phi_1^{\mathrm{A}}}\gamma_{\mathrm{gsf}} - \frac{1}{2}\partial_{\phi_2^{\mathrm{A}}}\gamma_{\mathrm{gsf}} \tag{25}$$

The second way to obtain γ_{gsf} is via a truncated Fourier series. In $\mathrm{PFDD_{fs}}$, γ_{gsf} takes the form [32]

$$\gamma_{\mathrm{gsf}} = \sum_{i=1}^{N_{\mathrm{fs}}} c_i f_i \tag{26}$$

where N_{fs} is the number of terms in the truncated Fourier series, f_i are trigonometric functions of all order parameters on the same slip plane, and coefficients c_i are related to N_{fs} selected γ_{gsf} values taken from the GSFE surface. In the literature, $N_{\mathrm{fs}} = 3$ [34], 6 [15], 7 [27, 32], 8 [35], 12 [36], or 16 [37]. In particular, the 7-term Fourier series is by far the most popular choice for pure FCC metals [16, 38, 39] and has been employed in all previous PFDD simulations. The seven points on the GSFE surface, A, G, G_1, G_2, G_3, T, and T_1, are illustrated in Fig. 3(a–b). In terms of $(\phi_{\bar{1}10}, \phi_{\bar{1}\bar{1}2})$, A lies at the origin; T and G are located at $(0.5, 0)$ and $(0.5, 0.5/3)$, respectively; T_1 lies half-way between A and T; and G_1, G_2, and G_3 are evenly spaced between A and G. The choice of these seven points is justified by the fact that half of the actual extended edge and screw dislocation paths lie within the triangle AGT.

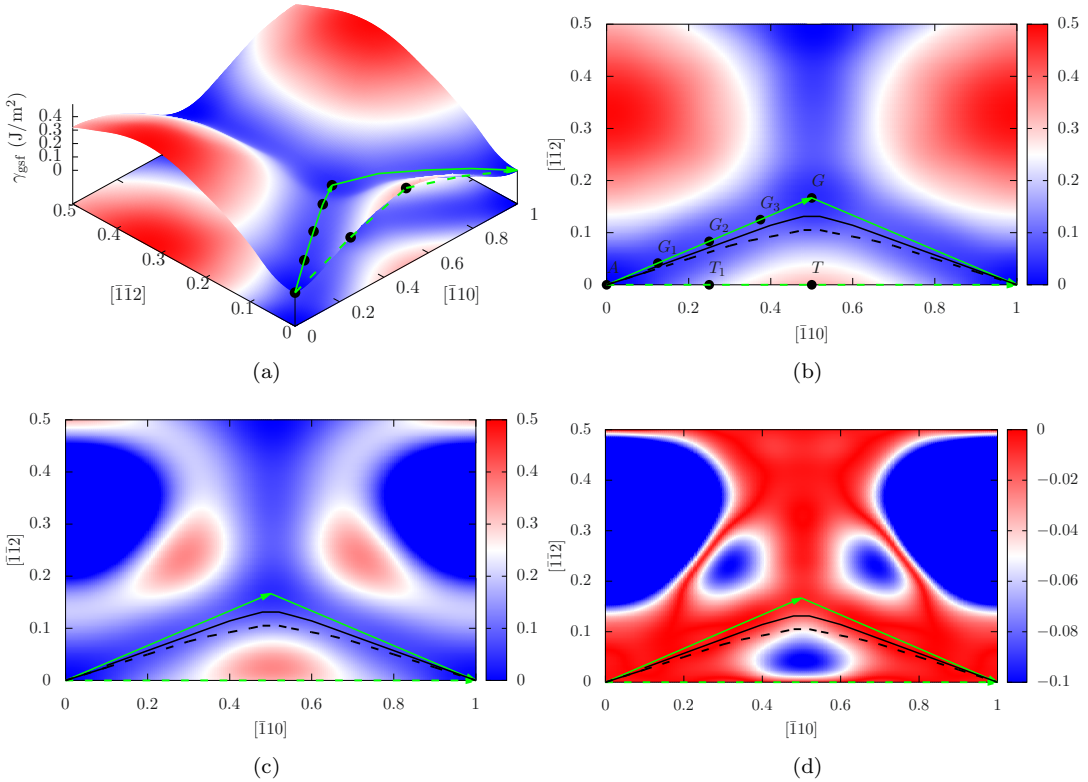

Figure 3. (a) 3D relaxed GSFE surface in a look-up table form on a (111) plane along both $[\bar{1}\bar{1}2]$ and $[\bar{1}10]$ directions. (b) is the projection of (a) onto the (111) plane. The seven points selected to fit the 7-term Fourier series [32] are highlighted in (a) and (b). (c) GSFE surface based on the 7-term Fourier series and (d) its difference with respect to the look-up table form. In (b–d), the solid and dashed black curves illustrate the actual paths for extended edge and screw dislocations, respectively [33]. All results are based by an EAM potential for Au [28], with γ_{gsf} in units of J/m^2. The solid and dashed green arrows represent the paths of Shockley partial dislocations and perfect dislocations, respectively.

With respect to the look-up table form, the 7-term Fourier series-based GSFE surface has two main drawbacks: (i) local energy minima are predicted in some regions that should be an energy maximum, as shown in Fig. 3(c), and (ii) the three points (G_1, G_2, and G_3) between A and G may not be sufficient to describe a complex GSFE curve along the $\langle 112 \rangle$ direction. To overcome these drawbacks, which are especially pronounced in Au, we propose an 11-term Fourier series. First, we identify four additional points on the GSFE surface: M, M_1, G_4, and G_5, which are shown in Fig. 4(a). In terms of $(\phi_{\bar{1}10}, \phi_{\bar{1}\bar{1}2})$, M is at the previous artificial local minimum (0,1/3); M_1 is in the middle of A and M; G_4 is in the middle of G_1 and G_2; and G_5 is in the middle of G_2 and G_3. Since, with respect to the origin A, all four new points are along the mirror-symmetric $\langle 112 \rangle$ direction, four additional cosines [37], associated with four coefficients c_7, c_8, c_9, and c_{10}, are added to the original 7-term Fourier series [32], i.e.,

$$\begin{aligned}\gamma_{gsf} = c_0 &+ c_1[\cos(2py) + \cos(py + qz) + \cos(py - qz)] \\ &+ c_2[\cos(2qz) + \cos(3py + qz) + \cos(3py - qz)] \\ &+ c_3[\cos(4py) + \cos(2py + 2qz) + \cos(2py - 2qz)] \\ &+ c_4[\cos(py + 3qz) + \cos(py - 3qz) + \cos(4py + 2qz) \\ &\quad + \cos(4py - 2qz) + \cos(5py + qz) + \cos(5py - qz)]\end{aligned}$$

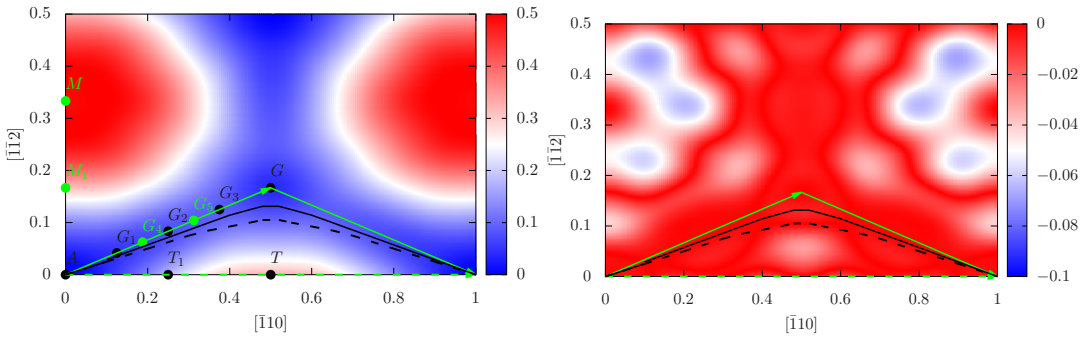

(a) (b)

Figure 4. (a) GSFE surface based on the 11-term Fourier series and (b) its difference with respect to the look-up table form in Fig. 3(b). In (a), the four additional points with respect to the 7-term Fourier series are highlighted in green. Results are based on an EAM potential for Au [28], with the energies in units of J/m^2.

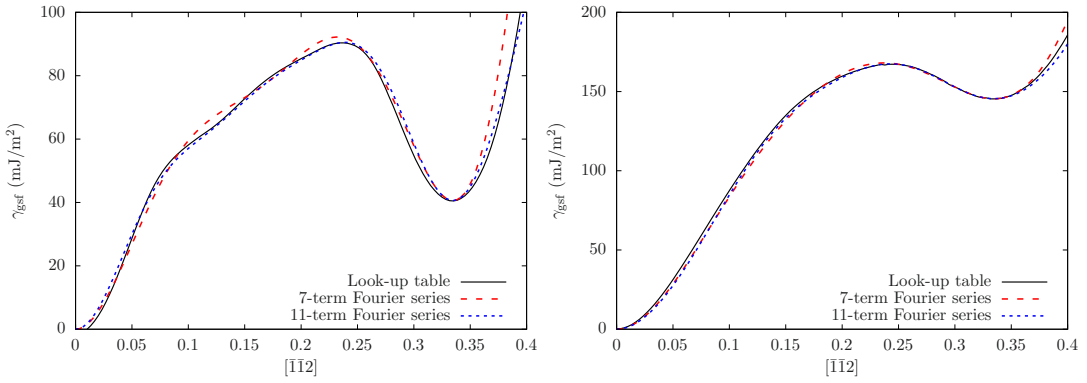

(a) Au (b) Al

Figure 5. The GSFE curve along the $[\bar{1}\bar{1}2]$ direction given by the look-up table form, the 7-term Fourier series form, and the 11-term Fourier series form for (a) Au and (b) Al.

$$
\begin{aligned}
&+c_5[\sin(2py) - \sin(py+qz) - \sin(py-qz)] \\
&+c_6[\sin(4py) - \sin(2py+2qz) - \sin(2py-2qz)] \\
&+c_7[\cos(6py) + \cos(3py+3qz) + \cos(3py-3qz)] \\
&+c_8[\cos(8py) + \cos(4py+4qz) + \cos(4py-4qz)] \\
&+c_9[\cos(4qz) + \cos(6py+2qz) + \cos(6py-2qz)] \\
&+c_{10}[\cos(6qz) + \cos(9py+3qz) + \cos(9py-3qz)] \qquad (27)
\end{aligned}
$$

where $p = 2\pi/(\sqrt{3}b^{\mathrm{P}})$ and $q = 2\pi/b^{\mathrm{P}}$ are magnitudes of the reciprocal lattice vectors [32], $y = \phi_2^{\mathrm{A}} b_2^{\mathrm{A}}$, and $z = \phi_1^{\mathrm{A}} b_1^{\mathrm{A}}$. In Au, with respect to the look-up table form, the errors in the Fourier series-based GSFE surface are significantly smaller for the 11-term Fourier series form than the original 7-term one, as shown in Figs. 3(d) and 4(b). In particular, the GSFE curve along the $[\bar{1}\bar{1}2]$ direction given by the 11-term Fourier series form is more accurate, as shown in Fig. 5(a). With the help of Eqs. 15 and 16, Eq. 27 can be written as a function of the three order parameters in $\mathrm{PFDD_{fs}}$, i.e.,

$$
\begin{aligned}
\gamma_{\mathrm{gsf}} = {} & c_0 + c_1[\cos 2\pi(\phi_2^{\mathrm{P}} - \phi_3^{\mathrm{P}}) + \cos 2\pi(\phi_3^{\mathrm{P}} - \phi_1^{\mathrm{P}}) + \cos 2\pi(\phi_1^{\mathrm{P}} - \phi_2^{\mathrm{P}})] \\
& + c_2[\cos 2\pi(2\phi_1^{\mathrm{P}} - \phi_2^{\mathrm{P}} - \phi_3^{\mathrm{P}}) + \cos 2\pi(2\phi_3^{\mathrm{P}} - \phi_1^{\mathrm{P}} - \phi_2^{\mathrm{P}}) + \cos 2\pi(2\phi_2^{\mathrm{P}} - \phi_1^{\mathrm{P}} - \phi_3^{\mathrm{P}})]
\end{aligned}
$$

$$
\begin{aligned}
&+c_3[\cos 4\pi(\phi_2^{\mathrm{P}}-\phi_3^{\mathrm{P}})+\cos 4\pi(\phi_3^{\mathrm{P}}-\phi_1^{\mathrm{P}})+\cos 4\pi(\phi_1^{\mathrm{P}}-\phi_2^{\mathrm{P}})]\\
&+c_4[\cos 2\pi(3\phi_1^{\mathrm{P}}-\phi_2^{\mathrm{P}}-2\phi_3^{\mathrm{P}})+\cos 2\pi(3\phi_1^{\mathrm{P}}-2\phi_2^{\mathrm{P}}-\phi_3^{\mathrm{P}})+\cos 2\pi(2\phi_1^{\mathrm{P}}+\phi_2^{\mathrm{P}}-3\phi_3^{\mathrm{P}})\\
&\quad+\cos 2\pi(2\phi_1^{\mathrm{P}}-3\phi_2^{\mathrm{P}}+\phi_3^{\mathrm{P}})+\cos 2\pi(\phi_1^{\mathrm{P}}+2\phi_2^{\mathrm{P}}-3\phi_3^{\mathrm{P}})+\cos 2\pi(\phi_1^{\mathrm{P}}-3\phi_2^{\mathrm{P}}+2\phi_3^{\mathrm{P}})]\\
&+c_5[\sin 2\pi(\phi_2^{\mathrm{P}}-\phi_3^{\mathrm{P}})+\sin 2\pi(\phi_3^{\mathrm{P}}-\phi_1^{\mathrm{P}})+\sin 2\pi(\phi_1^{\mathrm{P}}-\phi_2^{\mathrm{P}})]\\
&+c_6[\sin 4\pi(\phi_2^{\mathrm{P}}-\phi_3^{\mathrm{P}})+\sin 4\pi(\phi_3^{\mathrm{P}}-\phi_1^{\mathrm{P}})+\sin 4\pi(\phi_1^{\mathrm{P}}-\phi_2^{\mathrm{P}})]\\
&+c_7[\cos 6\pi(\phi_2^{\mathrm{P}}-\phi_3^{\mathrm{P}})+\cos 6\pi(\phi_3^{\mathrm{P}}-\phi_1^{\mathrm{P}})+\cos 6\pi(\phi_1^{\mathrm{P}}-\phi_2^{\mathrm{P}})]\\
&+c_8[\cos 8\pi(\phi_2^{\mathrm{P}}-\phi_3^{\mathrm{P}})+\cos 8\pi(\phi_3^{\mathrm{P}}-\phi_1^{\mathrm{P}})+\cos 8\pi(\phi_1^{\mathrm{P}}-\phi_2^{\mathrm{P}})]\\
&+c_9[\cos 4\pi(2\phi_1^{\mathrm{P}}-\phi_2^{\mathrm{P}}-\phi_3^{\mathrm{P}})+\cos 4\pi(\phi_1^{\mathrm{P}}+\phi_2^{\mathrm{P}}-2\phi_3^{\mathrm{P}})+\cos 4\pi(\phi_1^{\mathrm{P}}-2\phi_2^{\mathrm{P}}+\phi_3^{\mathrm{P}})]\\
&+c_{10}[\cos 6\pi(2\phi_1^{\mathrm{P}}-\phi_2^{\mathrm{P}}-\phi_3^{\mathrm{P}})+\cos 6\pi(\phi_1^{\mathrm{P}}+\phi_2^{\mathrm{P}}-2\phi_3^{\mathrm{P}})+\cos 6\pi(\phi_1^{\mathrm{P}}-2\phi_2^{\mathrm{P}}+\phi_3^{\mathrm{P}})]
\end{aligned}
\tag{28}
$$

Table 3. Locations and values of γ_{gsf} (in $\mathrm{mJ/m^2}$) for the eleven selected points (Fig. 4(a)) on the GSFE surface calculated from the EAM potentials for Au [28] and Al [29].

	$\phi_{\bar{1}10}$	$\phi_{\bar{1}\bar{1}2}$	γ_{gsf} (Au)	γ_{gsf} (Al)
A	0	0	0	0
T_1	1/4	0	184.2	212.7
T	1/2	0	323.3	395.1
G_1	1/8	1/24	51.3	65.3
G_4	3/16	1/16	64.3	112.5
G_2	1/4	1/12	77.2	144.2
G_5	5/16	5/48	86.8	161.9
G_3	3/8	1/8	89.4	167.1
G	1/2	1/6	40.6	145.4
M_1	0	1/6	314.1	392.9
M	0	1/3	493.5	576.4

Fitting Eq. 27 or Eq. 28 to the positions of the eleven points yields

$$
\begin{aligned}
c_0 &= 0.106G+0.719G_1-0.108G_2-0.344G_3-0.758G_4+0.758G_5+0.202T\\
&\quad+0.375T_1+0.108M+0.094M_1 &(29)\\
c_1 &= -0.043G-0.092G_1+0.083G_2+0.092G_3+0.320G_4-0.32G_5-0.112T\\
&\quad-0.083M+0.028M_1 &(30)\\
c_2 &= -0.059G-0.035G_1+0.142G_2+0.461G_3+0.175G_4-0.528G_5-0.071T\\
&\quad-0.25T_1+0.072M+0.017M_1 &(31)\\
c_3 &= 0.044G+0.24G_1-0.083G_2-0.24G_3-0.253G_4+0.253G_5+0.171T\\
&\quad-0.028M-0.088M_1 &(32)\\
c_4 &= -0.02G+0.046G_1-0.046G_3-0.16G_4+0.16G_5-0.028T+0.028M_1 &(33)\\
c_5 &= 0.144G+0.144G_2-0.144M-0.144M_1 &(34)\\
c_6 &= -0.048G+0.144G_2+0.048M-0.144M_1 &(35)\\
c_7 &= 0.115G+0.092G_1-0.011G_2-0.342G_3-0.32G_4+0.32G_5-0.013T\\
&\quad+0.25T_1+0.011M-0.1M_1 &(36)\\
c_8 &= -0.072G-0.24G_1+0.24G_3+0.253G_4-0.253G_5-0.005T+0.005M_1 &(37)\\
c_9 &= -0.008G-0.24G_1+0.119G_2+0.115G_3+0.253G_4-0.253G_5+0.016T\\
&\quad-0.125T_1-0.008M+0.052M_1 &(38)
\end{aligned}
$$

$$c_{10} = 0.028G - 0.058G_1 - 0.214G_2 - 0.119G_3 + 0.145G_4 + 0.208G_5 + 0.001T \quad (39)$$

Note that these equations only apply to the 11-term Fourier series form, not the 7-term Fourier series one, for which the coefficients were presented in Ref. [16]. Locations and values of γ_{gsf} for the eleven selected points on the GSFE surface are summarized in Tab. 3. It follows that $\partial_{\phi_\alpha}\gamma_{\text{gsf}}$ is calculated by taking the partial derivative of γ_{gsf} with respect to each order parameter ϕ_α^{P} in Eq. 28. In this paper, both 7-term and 11-term Fourier series forms are applied to investigate disregistry profiles of dislocations in PFDD_{fs}.

3.4. *Gradient energy density* ψ_{gra}

Table 4. Values of the three parameters in Eq. 10 for Au and Al determined from the MS simulations of an extended edge monopole as discussed in the text. Note that α_{g0} is unitless.

	$g_0/(\mu d_{111})$	l_0/d_{111}	α_{g0}
Au	0.0547	9.62	0.8264
Al	0.0626	6.17	0.8294

The gradient energy density is included only in APFM. The values of the three parameters in Eq. 10 are presented in Tab. 4. These were fit from MS simulations of an extended edge monopole.

4. Simulation set-up

In this section, we present the set-up used in both the MS and PF-based simulations for static extended dislocations of pure edge or pure screw type. A dislocation dipole consisting of two dislocations of the same type but with opposite Burgers vector is built into a 3D periodic simulation box, which has lattice orientations

$$(\boldsymbol{i}_x, \boldsymbol{i}_y, \boldsymbol{i}_z) = \left(\frac{\sqrt{2}}{2}[\bar{1}10], \frac{\sqrt{3}}{3}[111], \frac{\sqrt{6}}{6}[11\bar{2}]\right) \quad (40)$$

for the edge dislocation dipole, and

$$(\boldsymbol{i}_x, \boldsymbol{i}_y, \boldsymbol{i}_z) = \left(\frac{\sqrt{6}}{6}[\bar{1}\bar{1}2], \frac{\sqrt{3}}{3}[111], \frac{\sqrt{2}}{2}[\bar{1}10]\right) \quad (41)$$

for the screw dislocation dipole. Let L_x, L_y, and L_z be the edge length of the simulation box along the x, y, and z directions, respectively. Within each dipole, the two dislocation lines are along the z axis, lie on the x-z plane, and are separated by $L_x/2$ along the x direction. In all simulations, larger L_x, L_y, and L_z were tested and the results were unchanged. The calculated 2D disregistry fields of one dislocation, which is referred to as a monopole in what follows, will be compared in Section 5.1.

4.1. *MS simulations*

All MS simulations in this work are carried out with LAMMPS [40]. The simulation box sizes, in units of d_{111}, are as follows: $L_x = 120\sqrt{6}$, $L_y = 180$, and $L_z = 9\sqrt{2}/2$ for the edge dislocation dipole, and $L_x = 180\sqrt{2}$, $L_y = 180$, and $L_z = 3\sqrt{6}$ for the screw dislocation dipole. The two types of boxes contain the same number of 259200 atoms. In order to quantitatively compare the simulation results, in MS calculations, we use the same EAM potentials [28, 29] as used for all material properties needed in the PF free energy model.

In each simulation, the energy of the dislocation-free system is first minimized via conjugate gradient relaxation. Then an undissociated perfect dislocation dipole is created by applying the corresponding isotropic elastic displacement fields to all atoms [25]. Under zero stress, we apply two types of relaxation methods in sequence, the first being the fast inertial relaxation engine (FIRE) [41] and the second the conjugate gradient method, during which each perfect dislocation monopole extends on its glide plane. The FIRE relaxation is conducted by 2500 steps. The conjugate gradient-based minimization iterations are terminated when one of the following two criteria is satisfied: (i) the energy change between successive iterations divided by the most recent energy magnitude is less than or equal to 10^{-15} and (ii) the length of the global force vector for all atoms is less than or equal to 10^{-15}.

4.2. *PF-based simulations*

A structured grid with uniform grid spacing h is employed, where $h = d_{111} = a_0/\sqrt{3}$ in APFM and APFM_{ng} while $h = b^{\text{P}} = a_0/\sqrt{2}$ in PFDD and PFDD_{fs}. The numbers of grid points along the x, y, and z directions are 294, 180, and 7, respectively, in APFM and APFM_{ng}, and 128 in all three directions in PFDD and PFDD_{fs}. The elastic energy density ψ_{ela} is calculated by the 3D fast Fourier transform method with the help of Green's functions. Following the MS simulations, an undissociated perfect dislocation dipole is inserted by assigning non-zero ϕ_α to the grid points needed to achieve a given dislocation character. During recursively running the TDGL equation, in which the time step and mobility m_0 are 0.5 and 1, respectively, each dislocation monopole becomes extended. Iterations are terminated when the change in the Euclidean norm of global vector of each order parameter between successive iterations is smaller than 10^{-3}. Parallel simulations starting from fully dissociated dislocations are also run and the results are almost identical, suggesting that the final relaxed dislocation structures are likely independent of the initial configuration and energy minimization path. Note that in APFM, the three parameters in Tab. 4 are determined from the MS-based Shockley partial dislocation core structures of a dissociated edge dislocation are used for both edge and screw dislocation dipoles. Note that in the current case of only one slip plane, $\boldsymbol{b}_1 \cdot \boldsymbol{b}_2 = 0$ in APFM, and so $\boldsymbol{N}_{12} = \boldsymbol{0}$ according to Eq. 9, suggesting that the interactions between different order parameters are not considered in calculating the gradient energy density.

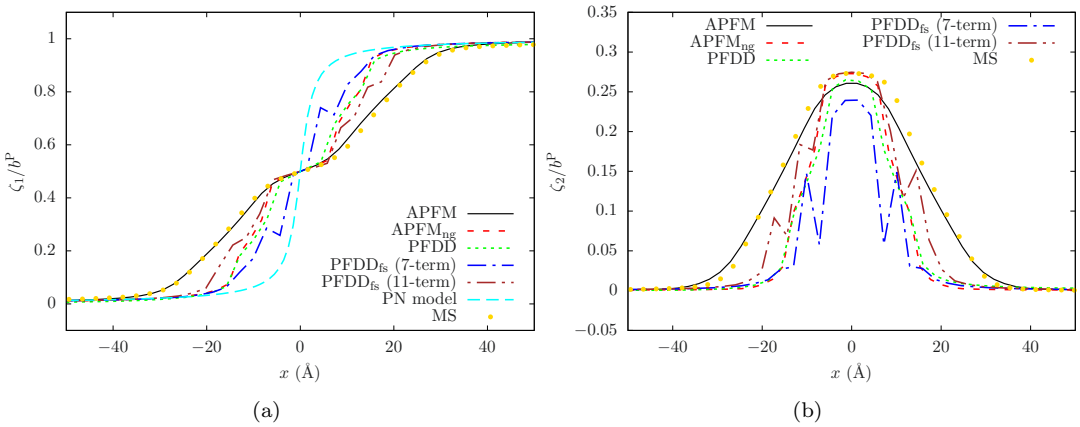

Figure 6. Disregistry fields of an edge monopole in Au (a) along and (b) normal to the perfect dislocation Burgers vector direction.

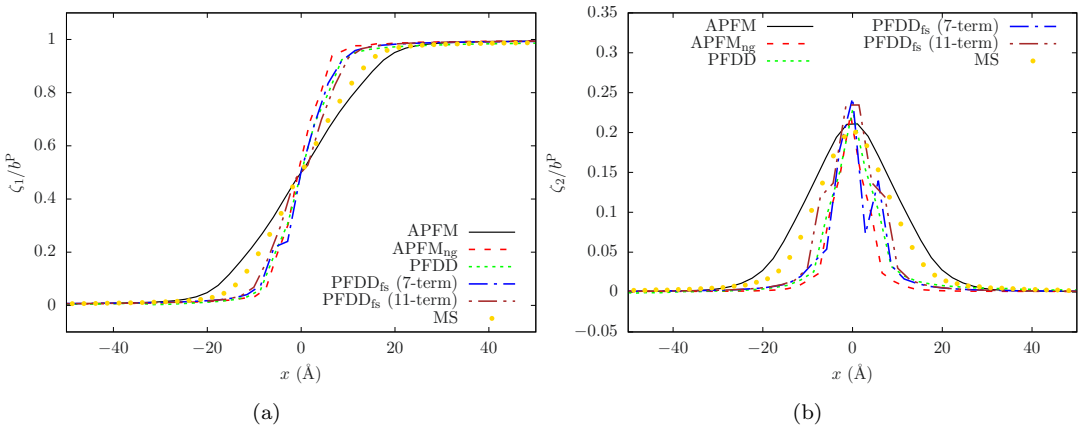

Figure 7. Disregistry fields of a screw monopole in Au (a) along and (b) normal to the perfect dislocation Burgers vector direction.

5. Results and discussions

5.1. *Comparison of the disregistry fields*

In this section, the disregistry profiles both along and normal to the perfect dislocation Burgers vector direction based on MS and different PF-based simulations are compared. In what follows, these two disregistry fields are denoted as ζ_1 and ζ_2, respectively. In MS, the disregistry vector $\boldsymbol{\zeta}$ (Eq. 2) is projected onto the two directions. In PF-based methods [16], for a given slip plane,

$$\zeta_\beta = \sum_{\alpha=1}^{n_{\text{sp}}} \phi_\alpha \boldsymbol{b}_\alpha \cdot \boldsymbol{s}_\beta \tag{42}$$

where n_{sp} is the total number of order parameters on the slip plane within which the αth order parameter and β direction lie. For edge monopoles, the results are also compared against the classical PN model, which was the first analytic model of the 1D disregistry field of a perfect dislocation along the Burgers vector direction x, i.e.,

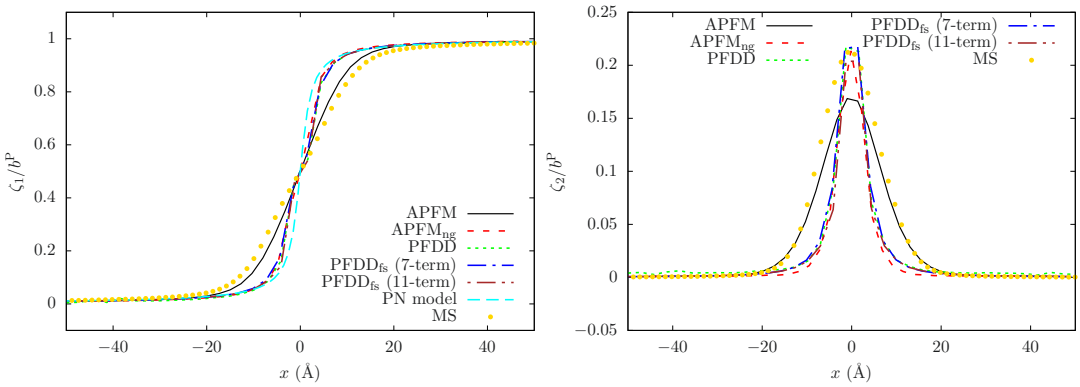

Figure 8. Disregistry fields of an edge monopole in Al (a) along and (b) normal to the perfect dislocation Burgers vector direction.

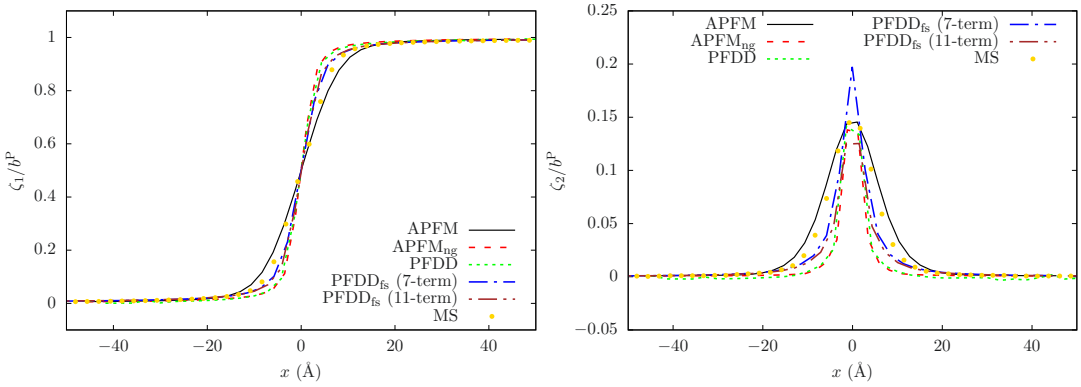

Figure 9. Disregistry fields of a screw monopole in Al (a) along and (b) normal to the perfect dislocation Burgers vector direction.

[42, 43],

$$\zeta_{\mathrm{PN}}(x) = \frac{b^{\mathrm{P}}}{\pi} \arctan \frac{2x(1-\nu)}{d_{111}} + \frac{b^{\mathrm{P}}}{2} \tag{43}$$

where $\nu = \lambda/[2(\lambda+\mu)]$ is the isotropic Poisson's ratio of the material, with μ and λ determined by Eqs. 17 and 18. Figs. 6–9 show that the PF-based disregistry fields are systematically closer to the MS-based ones than the 1D PN model prediction. However, note that there are a few aphysical local extrema on the PFDD$_{\mathrm{fs}}$-based disregistry profiles in Au. Specifically, this is the case in all four profiles when the 7-term Fourier series form is used to approximate γ_{gsf}, except ζ_1 of the screw monopole. On the other hand, only one disregistry profile, i.e., ζ_2 of the edge monopole, contains the aphysical local extrema if the 11-term Fourier series form is adopted for γ_{gsf}. Therefore, the aphysical PFDD$_{\mathrm{fs}}$-based results are likely attributed to the failure of the Fourier series forms to correctly reproduce the GSFE surface. Note that the aphysical local extrema do not exist in any disregistry profile in Al in this work, nor in previous PFDD$_{\mathrm{fs}}$ results when the 7-term Fourier series form was fit to *ab initio* calculation-informed GSFE data [30].

In the next two subsections, all results are compared in terms of two characteristics: the ISF width and the Shockley partial dislocation core size.

5.2. *Intrinsic stacking fault width*

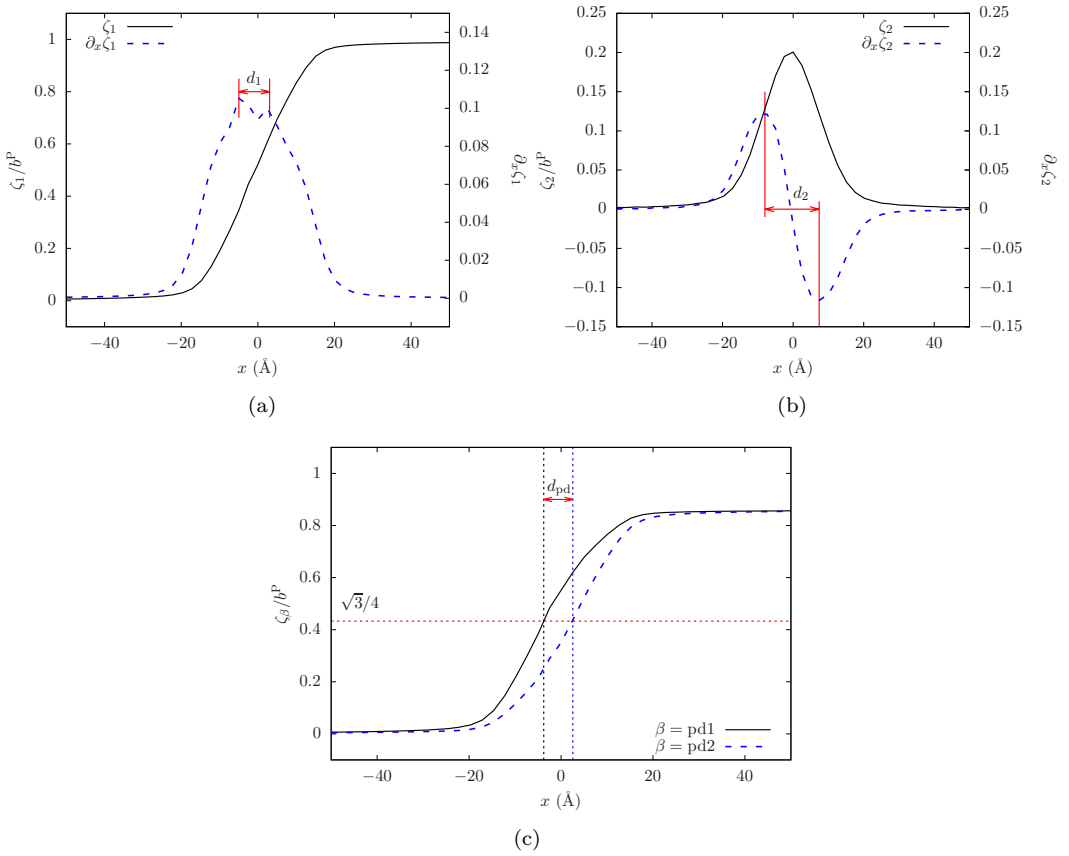

Figure 10. Different measurements d_ξ with $\xi = 1, 2, \mathrm{pd}$ of the ISF width based on MS diregistry fields for a screw monopole in Au.

The ISF width is a key parameter in quantifying the ISF structure associated with an extended dislocation and is directly comparable with experiments [44], which sometimes use the ISF width to determine the stable SFE of the material [45, 46]. Here, we discuss different methods to determine the ISF width, d_ξ, with ξ denoting a specific method.

In the continuum context, a dislocation can be represented as a continuous dislocation array with infinitesimal Burgers vectors. Accordingly, the derivative of the disregistry along the Burgers vector direction with respect to the coordinates, i.e., $\partial_x\zeta_1$, is the Burgers vector density [47]. The classical PN model (Eq. 43) does not consider dislocation dissociation and so the corresponding $\partial_x\zeta_1$ profile only has one peak. Later, the 1D PN model was advanced to treat extended dislocations [48] and when employed, two peaks emerge in the disregistry density profile. Particularly in FCC metals, analogous to the single peak in the classical PN model for the perfect dislocation center, the two peaks of $\partial_x\zeta_1$ in the extended PN model are assumed to correspond to the centers of the two Shockley partial dislocations and their separation distance is the ISF width d_1, as illustrated in Fig. 10(a). If the disregistry fields are

2D [27], two similar peaks exist for $\partial_x\zeta_2$, between which is d_2, as shown in Fig. 10(b). All derivatives here are approximated by the central difference method. For an edge monopole, d_1 and d_2 represent the distances between the edge and screw components, respectively and vice versa for a screw monopole.

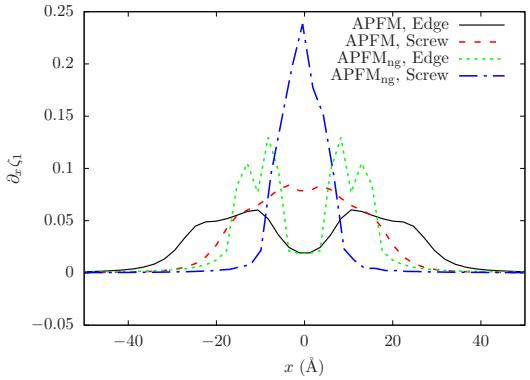

Figure 11. Partial derivative of the disregistry fields ζ_1 with respect to the coordinates x for an edge or a screw monopole in Au calculated by APFM and APFM$_{ng}$. APFM$_{ng}$ results show that (i) the screw monopole has only one maximum $\partial_x\zeta_1$ in total and (ii) there are two local maxima $\partial_x\zeta_1$ on each side of the perfect dislocation center for an edge monopole. In the first case, the dislocation is "undissociated" and so $d_1^{\text{scr}} = 0$. In the second case, the center of the Shockley partial dislocation core, and hence the ISF width d_1^{edg}, is not unique.

The determination of d_1 and d_2 is based on an assumption that there are two local maxima $\partial_x\zeta_\beta$ in total, each on different sides of the perfect dislocation center. However, in some cases, e.g., those shown in Fig. 11, either there is only one maximum $\partial_x\zeta_\beta$ in total or there are more than one local maximum $\partial_x\zeta_\beta$ on the same side of the perfect dislocation center. In the first case, the dislocation may be considered as "undissociated" and thus $d = 0$. In the second case, the location of the partial dislocation core center, and hence the ISF width, are not unique. This ambiguity originates from the physical and/or numerical noise in the calculations of the disregistry fields ζ_β. The noise is then amplified in $\partial_x\zeta_\beta$ during the numerical differentiation process. We found that the noise in $\partial_x\zeta_\beta$ is much greater in molecular dynamics simulations at 25 K than that in MS. Moreover, due to the combined effect of the elastic anisotropy of the material and that in the same monopole the edge and screw components of the two partial dislocations interact with each other differently, d_1 and d_2 are usually different, which adds to the uncertainty in determining the ISF widths.

For these reasons, we resort to two new methods that (i) only use the disregistry fields without taking derivatives and (ii) combine ζ_1 and ζ_2 into a single functional form. The first method projects ζ_1 and ζ_2 along the directions of the two partial dislocations, i.e.,

$$\zeta_{\text{pd1}} = \zeta_1 \cos 30^\circ + \zeta_2 \sin 30^\circ \tag{44}$$

$$\zeta_{\text{pd2}} = \zeta_1 \cos 30^\circ - \zeta_2 \sin 30^\circ \tag{45}$$

each of which ranges between 0 and $(\sqrt{3}/2)b^{\text{P}}$, as shown in Fig. 10(c). Taking $\zeta_1 = 0.5b^{\text{P}}$ as the perfect dislocation center, the two points with $\zeta_{\text{pd}} = (\sqrt{3}/4)b^{\text{P}}$ are assumed to correspond to the centers of the two Shockley partial dislocations, between which the ISF width is measured as d_{pd}.

The second approach is based on the ISF width in MS simulations identified by CNA [13], i.e., the width of the region with red atoms in Fig. 1. First, we build an ISF

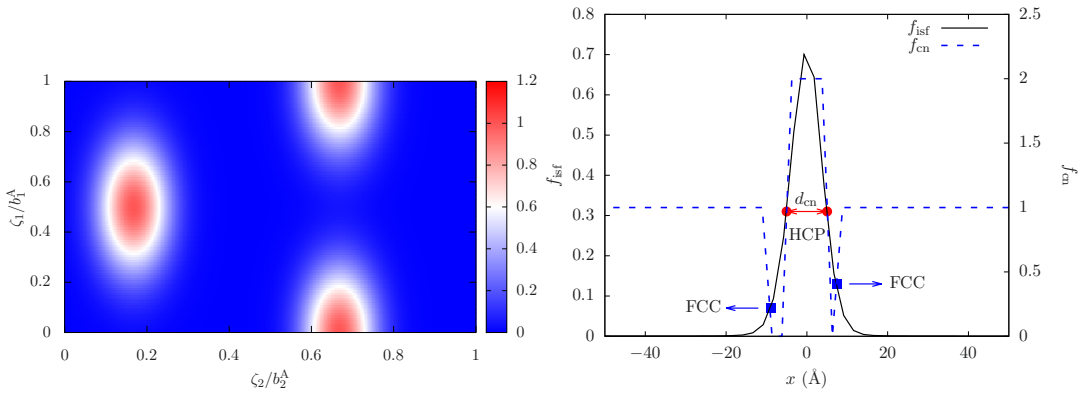

Figure 12. (a) $f_{\mathrm{isf}}(\zeta_1, \zeta_2)$ with $\epsilon = 15$. (b) Calculation of d_{cn} for a dissociated screw monopole in Au in an MS simulation based on $f_{\mathrm{isf}}[\zeta_1(x), \zeta_2(x)]$ and $f_{\mathrm{cn}}(x)$ [13]. In particular, $f_{\mathrm{isf}}(x) < 0.1$, $0.1 < f_{\mathrm{isf}}(x) < 0.31$, and $f_{\mathrm{isf}}(x) > 0.31$ correspond to FCC, disordered, and HCP local structures, respectively. d_{cn} is the distance between the two middle intersections (red circles) formed between the $f_{\mathrm{isf}}(x)$ and $f_{\mathrm{cn}}(x)$ profiles.

detection function, i.e.,

$$
\begin{aligned}
f_{\mathrm{isf}}(\zeta_1, \zeta_2) = \exp & \left[-\epsilon \left(\frac{\zeta_1}{b_1^{\mathrm{A}}} \right)^2 - 9\epsilon \left(\frac{\zeta_2}{b_2^{\mathrm{A}}} - \frac{2}{3} \right)^2 \right] \\
+ \exp & \left[-\epsilon \left(\frac{\zeta_1}{b_1^{\mathrm{A}}} - \frac{1}{2} \right)^2 - 9\epsilon \left(\frac{\zeta_2}{b_2^{\mathrm{A}}} - \frac{1}{6} \right)^2 \right] \\
+ \exp & \left[-\epsilon \left(\frac{\zeta_1}{b_1^{\mathrm{A}}} - 1 \right)^2 - 9\epsilon \left(\frac{\zeta_2}{b_2^{\mathrm{A}}} - \frac{2}{3} \right)^2 \right]
\end{aligned}
\tag{46}
$$

which consists of a sum of Gaussian functions about the states $(\zeta_1/b_1^{\mathrm{A}}, \zeta_2/b_2^{\mathrm{A}}) = (0, 2/3), (1/2, 1/6), (1, 2/3)$ that correspond to the ISFs on a GSFE surface, as shown in Fig. 12(a). For relatively smooth Gaussian functions, $\epsilon = 15$.

Table 5. The HCP region threshold κ that is used to determine d_{cn} based on $f_{\mathrm{isf}}(x)$ for different monopoles in Au and Al.

	Au, Edge	Au, Screw	Al, Edge	Al, Screw
κ	0.48	0.31	0.374	0.31

Next, the MS-based disregistry fields $[\zeta_1(x), \zeta_2(x)]$ are substituted into Eq. 46. This action results in $f_{\mathrm{isf}}(x)$ that can be plotted against the CNA index $f_{\mathrm{cn}}(x)$, where $f_{\mathrm{cn}} =$ 0, 1, and 2 correspond to disordered, FCC, and HCP local structures, respectively. Four intersections form between the two curves, labeled by the two blue squares and two red circles in Fig. 12(b), which can be considered the transitions between the FCC and disordered regions as well as those between the disordered and HCP regions, respectively. The values of f_{isf} at the two intersections nearest to the perfect dislocation center, i.e., the two red circles, are averaged to yield the HCP region threshold κ. It follows that for a given PF-based $f_{\mathrm{isf}}(x)$ profile, the distance between the two points associated with $f_{\mathrm{isf}} > \kappa$ is the ISF width d_{cn}. Note that the intersections, and hence the threshold κ, depend on the relative scaling between f_{isf} and f_{cn}. Thus, for each

monopole, the value of κ, presented in Tab. 5, is determined by fitting to the MS-based ISF width rendered by CNA (Fig. 1).

Table 6. ISF width measures, in units of d_{111}, for Au and Al. In PFDD_{fs}, both 7-term and 11-term Fourier series forms are used to obtain the GSFE surface γ_{gsf}; some results for Au are presented as "–" when the disregistry field profiles contain aphysical local extrema. Superscripts edg and scr stand for edge and screw monopoles, respectively. Based on the numerical resolution, all APFM and APFM_{ng} results are in $\pm 0.5 d_{111}$, while all PFDD and PFDD_{fs} results are in $\pm 0.5 b^{\text{P}}$, respectively. † There are more than one local maximum $\partial_x \zeta_\beta$ on the same side of the perfect dislocation center. In this case, the largest local maximum $\partial_x \zeta_\beta$ on the same side of the perfect dislocation center is assumed to correspond to the Shockley partial dislocation core center. ‡ There is only one local maximum $\partial_x \zeta_1$ in total and hence $d_1 = 0$ by definition. § The maximum f_{isf} is smaller than the corresponding HCP region threshold κ and hence $d_{\text{cn}} = 0$ by definition.

		MS	APFM	APFM_{ng}	PFDD	PFDD_{fs}(7-term)	PFDD_{fs}(11-term)
Au	d_1^{edg}	11.9	10.0	6.0†	6.12†	–	7.35†
	d_2^{edg}	10.8	10.0	6.0†	6.12†	–	–
	$d_{\text{pd}}^{\text{edg}}$	9.53	8.55	6.14	5.11	2.52	6.6
	$d_{\text{cn}}^{\text{edg}}$	10.8	9.75	6.54	5.59	3.06	7.13
	d_1^{scr}	2.1	4.0	0‡	0‡	3.67	3.67
	d_2^{scr}	6.3	6.0	1.0	3.67	–	3.67
	$d_{\text{pd}}^{\text{scr}}$	2.63	3.34	1.07	1.38	1.19	2.38
	$d_{\text{cn}}^{\text{scr}}$	4.1	5.42	1.72	2.21	1.93	3.26
Al	d_1^{edg}	4.5	0‡	3.0	0‡	0‡	0‡
	d_2^{edg}	5.8	6.0	3.0	3.67	3.67	3.67
	$d_{\text{pd}}^{\text{edg}}$	2.69	1.72	1.25	1.77	1.71	1.69
	$d_{\text{cn}}^{\text{edg}}$	3.85	2.09	1.7	2.52	2.51	2.4
	d_1^{scr}	0‡	0‡	0‡	0‡	0‡	0‡
	d_2^{scr}	4.2	4.0	2.0	3.67	2.45	3.67
	$d_{\text{pd}}^{\text{scr}}$	1.13	1.2	0.47	0.54	0.87	0.58
	$d_{\text{cn}}^{\text{scr}}$	1.05	1.53	0§	0§	1.49	0§

Results of ISF widths d determined by different methods using MS and PF-based simulation data are summarized in Tab. 6. All methods find that the edge monopole has a larger ISF width than a screw monopole for the same material in agreement with linear elasticity. Also for the same type of monopole, the ISF width is larger in Au than in Al, between which the former has a lower stable SFE. Among the PF-based methods, there are three main differences:

(1) Between APFM and APFM_{ng}, introducing the gradient energy density ψ_{gra} uniformly increases the ISF width d in all cases where d is non-zero. This is an outcome revealed by the present calculations with the selected material parameters. We find that it is more energetically favorable for the dislocation to increase d, thereby reducing the interaction energy between the partial dislocation at the expense of increasing the fault area than the other way around. Note that this finding agrees with a prior PF-based work [49]. Moreover, varying η_{g0} to any non-zero value only affects the shapes of the disregistry profiles but not d [38].

(2) Between APFM_{ng} and PFDD, two essential differences are elastic anisotropy and grid spacing, the latter of which is negligible. It is found that when d is non-zero, d is larger in PFDD than in APFM_{ng}, except $d_{\text{pd}}^{\text{edg}}$ and $d_{\text{cn}}^{\text{edg}}$ in Au. Note that the elastic anisotropy index for cubic systems $A_{\text{c}} = 2C_{44}/(C_{11} - C_{12}) = 1.21$ and 2.9 for Al and Au, respectively [50]. The influence of the elastic anisotropy on the core structure of extended dislocations agrees with a recent analytic study in FCC metals [51].

(3) Between PFDD and PFDD_{fs}, γ_{gsf} is calculated in different ways. In Au, with

respect to the PFDD results, PFDD_{fs} tends to underestimate and overestimate d, respectively, when the 7-term and 11-term Fourier series forms are used to approximate γ_{gsf}. In Al, the PFDD_{fs} results with the 11-term Fourier series form for γ_{gsf} are generally more accurate than those based on the 7-term Fourier series form, especially for the screw monopole which has a narrow ISF.

5.3. *Shockley partial dislocation core size*

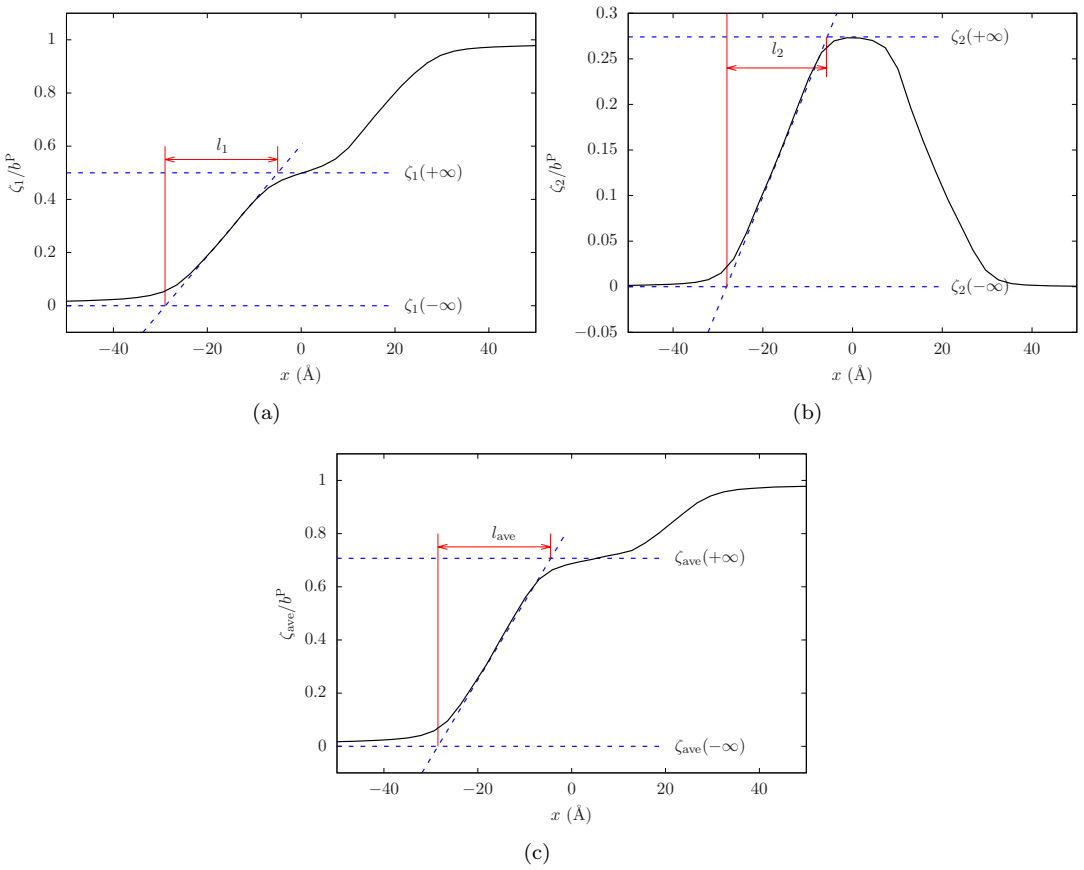

Figure 13. Different measurements l_ξ with $\xi = 1, 2, \text{ave}$ of a Shockley partial dislocation core size based on MS diregistry field for an edge monopole in Au.

Here, following the determination of the interface region width in Ref. [52], the core size of a Shockley partial dislocation is defined as

$$l_\beta = \frac{|\zeta_\beta(+\infty) - \zeta_\beta(-\infty)|}{|\partial_x \zeta_\beta(0)|} \tag{47}$$

where $x = 0$ corresponds to the location with maximum $\partial_x \zeta_\beta$, regardless of how many maximum $\partial_x \zeta_\beta$ there may be; $-\infty$ and $+\infty$ refer to the boundaries between the unslipped region and the partial dislocation and that between the partial dislocation and ISF, respectively. The measures l_1 and l_2 are depicted schematically in Fig. 13(a–b). Since, as in the case of the ISF widths, usually $l_1 \neq l_2$, we propose an averaged

Table 7. Shockley partial dislocation core size measures, in units of d_{111}, based on Eqs. 47 and 48 for Au and Al. Superscripts edg and scr stand for edge and screw monopole, respectively. Based on numerical resolution, all APFM-based results are $\pm 0.5 d_{111}$. Only APFM-based results are presented for that l_{ave} is used as l_0 in Eq. 10.

	Au			Al		
	MS	APFM	APFM_{ng}	MS	APFM	APFM_{ng}
l_1^{edg}	9.7	10.1	3.5	5.7	4.6	2.6
l_2^{edg}	8.2	9.7	3.4	4.3	4.9	2.2
$l_{\text{ave}}^{\text{edg}}$	9.6	10.4	3.6	6.2	6.4	2.9
l_1^{scr}	5.2	7.2	4.7	3.2	3.6	1.5
l_2^{scr}	6.0	7.6	2.9	3.5	4.2	1.3
$l_{\text{ave}}^{\text{scr}}$	7.1	8.7	2.8	4.7	5.4	2.4

disregistry profile, ζ_{ave}, i.e.,

$$\zeta_{\text{ave}} = \sqrt{(\zeta_1)^2 + 3\,(\zeta_2)^2} \tag{48}$$

which, along with the measurement of the core size l_{ave}, are shown in Fig. 13(c). In APFM, it is l_{ave} that is used as l_0 in Eq. 10. Values of l_ξ with $\xi = 1, 2, \text{ave}$ are summarized in Tab. 7 for Au and Al. Like the ISF widths, all results here indicate that adding the gradient energy density ψ_{gra} to the total energy density increases the partial dislocation core size and yields a better agreement with MS.

6. Conclusions

In this work, MS and PF-based methods are employed to calculate the 2D disregistry fields of extended dislocations with pure edge and pure screw characters in two FCC metals: Au and Al, which have distinct stable SFE and elastic anisotropy. Four PF-based methods, including APFM and PFDD methods as well as their variants, are employed. A new 11-term truncated Fourier series form is developed to better approximate the GSFE surface γ_{gsf} than the original 7-term one in that the former addresses the artificial local energy minimum in some regions and presents more accurate γ_{gsf} values in the region where actual paths for the extended dislocations cross. As a result, the aphysical local extrema on some disregistry profiles predicted by PFDD_{fs} with the 7-term Fourier series form for γ_{gsf} are removed in the 11-term Fourier series form-based PFDD_{fs} results. The general agreement between MS and PF-based simulations confirms the accuracy of using the elastic energy density ψ_{ela} and GSFE density ψ_{gsf} in the latter as approximations to the corresponding atomic quantities. Introducing the gradient energy ψ_{gra}, which is done in APFM, yields an improvement in the description of the dislocation core structure with respect to the MS-based results, compared with the PF-based methods without ψ_{gra}.

The differences in the calculated disregistry fields are quantified in terms of the ISF width d and the Shockley partial dislocation core size l. A common factor in determining d and l is the identification of the Shockley partial dislocation core center, whose location may not be unique if one assumes that it corresponds to a peak value in the partial derivative of the disregistry with respect to the coordinates along the direction that is on the slip plane and normal to the dislocation line. Accordingly, two

new methods, which make use of only the 2D disregistry fields but not their derivatives, are proposed to calculate d. We also propose one new method, which combines the disregistry fields along the two perpendicular directions, to determine l. It is found that, in general

(1) Adding ψ_{gra} to the total energy density increases both d and l, which help achieve better predictions of the entire dislocation structure with respect to MS;
(2) Approximating an elastic anisotropic medium as an elastic isotropic one results in an overestimate of d;
(3) Determining γ_{gsf}, and hence ψ_{gsf}, using either the 2D truncated Fourier series or the look-up table form, does not significantly affect the calculated disregistry fields as long as the key parameters in the Fourier series are based on the same interatomic potentials used in MS.

Ongoing work includes realizing full elastic anisotropy in PFDD, carrying out *ab initio*-based calculations to obtain more accurate GSFE surfaces for common metals, and extending the current work to other lattices such as HCP and body-centered cubic types. We will also compare the PF-based disregistry profiles with those from other meso-scale modeling methods, and compare the Shockley partial dislocation core center determination methods included in this work with other approaches based on the differential displacement map or Nye tensor.

Acknowledgement

We thank Dr. Yunzhi Wang and Dr. Vassili Vorontsov for helpful discussions. The work of SX was supported in part by the Elings Prize Fellowship in Science offered by the California NanoSystems Institute (CNSI) on the UC Santa Barbara campus. SX and IJB gratefully acknowledge support in part from the Office of Naval Research under contract ONR BRC Grant N00014-18-1-2392 and the Center for Scientific Computing from the CNSI, MRL: an NSF MRSEC (DMR-1720256) and NSF CNS-1725797. JRM and BS gratefully acknowledge partial support from the Deutsche Forschungsgemeinschaft (DFG) through Subproject M5 (M8) in the Priority Programme 1713. AH gratefully acknowledges support from the Los Alamos National Laboratory Directed Research and Development (LDRD) Program under the Project #20160156ER. This work used the Extreme Science and Engineering Discovery Environment (XSEDE), which is supported by National Science Foundation grant number ACI-1053575.

Disclosure

The authors declare no conflict of interest.

References

[1] S. Xu and X. Chen, *Modeling dislocations and heat conduction in crystalline materials: atomistic/continuum coupling approaches*, Int. Mater. Rev. 0 (2018), pp. 1–32, Available at https://doi.org/10.1080/09506608.2018.1486358.
[2] S. Xu, L. Xiong, Y. Chen, and D.L. McDowell, *An analysis of key characteristics of the Frank-Read source process in FCC metals*, J. Mech. Phys. Solids 96 (2016),

pp. 460–476, Available at http://www.sciencedirect.com/science/article/pii/S0022509616301016.

[3] S. Xu, R. Che, L. Xiong, Y. Chen, and D.L. McDowell, *A quasistatic implementation of the concurrent atomistic-continuum method for FCC crystals*, Int. J. Plast. 72 (2015), pp. 91–126, Available at http://www.sciencedirect.com/science/article/pii/S0749641915000777.

[4] S. Xu, L. Xiong, Y. Chen, and D.L. McDowell, *Validation of the concurrent atomistic-continuum method on screw dislocation/stacking fault interactions*, Crystals 7 (2017), p. 120, Available at http://www.mdpi.com/2073-4352/7/5/120.

[5] D. Chen and Y. Kulkarni, *Entropic interaction between fluctuating twin boundaries*, J. Mech. Phys. Solids 84 (2015), pp. 59–71, Available at http://www.sciencedirect.com/science/article/pii/S0022509615300065.

[6] J. Jung, J.I. Yoon, J.G. Kim, M.I. Latypov, J.Y. Kim, and H.S. Kim, *Continuum understanding of twin formation near grain boundaries of FCC metals with low stacking fault energy*, npj Comput. Mater. 3 (2017), p. 21, Available at https://www.nature.com/articles/s41524-017-0023-1.

[7] S. Xu, L. Xiong, Y. Chen, and D.L. McDowell, *Edge dislocations bowing out from a row of collinear obstacles in Al*, Scripta Mater. 123 (2016), pp. 135–139, Available at http://www.sciencedirect.com/science/article/pii/S135964621630272X.

[8] S. Xu, L. Xiong, Y. Chen, and D.L. McDowell, *Shear stress- and line length-dependent screw dislocation cross-slip in FCC Ni*, Acta Mater. 122 (2017), pp. 412–419, Available at http://www.sciencedirect.com/science/article/pii/S1359645416307601.

[9] T. Luo, P. Ming, and Y. Xiang, *From atomistic model to the Peierls-Nabarro model with γ-surface for dislocations*, Arch. Rational. Mech. Anal. 230 (2018), pp. 735–781, Available at https://link.springer.com/article/10.1007/s00205-018-1257-x.

[10] S. Xu, J. Rigelesaiyin, L. Xiong, Y. Chen, and D.L. McDowell, *Generalized continua concepts in coarse-graining atomistic simulations*, in *Generalized Models and Nonclassical Approaches in Complex Materials 2*, Advanced Structured Materials, Springer, Cham, 2018, pp. 237–260, Available at https://link.springer.com/chapter/10.1007/978-3-319-77504-3_12.

[11] S. Xu, L. Xiong, Y. Chen, and D.L. McDowell, *Sequential slip transfer of mixed-character dislocations across $\Sigma 3$ coherent twin boundary in FCC metals: a concurrent atomistic-continuum study*, npj Comput. Mater. 2 (2016), p. 15016, Available at http://www.nature.com/articles/npjcompumats201516.

[12] S. Xu, L. Xiong, Y. Chen, and D.L. McDowell, *Comparing EAM potentials to model slip transfer of sequential mixed character dislocations across two symmetric tilt grain boundaries in Ni*, JOM 69 (2017), pp. 814–821, Available at https://link.springer.com/article/10.1007/s11837-017-2302-1.

[13] A. Stukowski, *Structure identification methods for atomistic simulations of crystalline materials*, Modelling Simul. Mater. Sci. Eng. 20 (2012), p. 045021, Available at http://iopscience.iop.org/0965-0393/20/4/045021.

[14] G. Liu, X. Cheng, J. Wang, K. Chen, and Y. Shen, *Improvement of nonlocal Peierls-Nabarro models*, Comput. Mater. Sci. 131 (2017), pp. 69–77, Available at http://www.sciencedirect.com/science/article/pii/S0927025617300526.

[15] Y. Xiang, H. Wei, P. Ming, and W. E, *A generalized Peierls-Nabarro model for curved dislocations and core structures of dislocation loops in Al and Cu*, Acta Mater. 56 (2008), pp. 1447–1460, Available at http://www.sciencedirect.com/science/article/pii/S1359645407008087.

[16] A. Hunter, I.J. Beyerlein, T.C. Germann, and M. Koslowski, *Influence of the stacking fault energy surface on partial dislocations in fcc metals with a three-dimensional phase field dislocations dynamics model*, Phys. Rev. B 84 (2011), p. 144108, Available at https://link.aps.org/doi/10.1103/PhysRevB.84.144108.

[17] J.R. Mianroodi and B. Svendsen, *Atomistically determined phase-field modeling of dislocation dissociation, stacking fault formation, dislocation slip, and reactions in fcc systems*,

J. Mech. Phys. Solids 77 (2015), pp. 109–122, Available at http://www.sciencedirect.com/science/article/pii/S0022509615000162.

[18] Y.U. Wang, Y.M. Jin, A.M. Cuitiño, and A.G. Khachaturyan, *Nanoscale phase field microelasticity theory of dislocations: model and 3d simulations*, Acta Mater. 49 (2001), pp. 1847–1857, Available at http://www.sciencedirect.com/science/article/pii/S1359645401000751.

[19] M. Koslowski, A.M. Cuitiño, and M. Ortiz, *A phase-field theory of dislocation dynamics, strain hardening and hysteresis in ductile single crystals*, J. Mech. Phys. Solids 50 (2002), pp. 2597–2635, Available at http://www.sciencedirect.com/science/article/pii/S0022509602000376.

[20] N. Zhou, C. Shen, M.J. Mills, J. Li, and Y. Wang, *Modeling displacive-diffusional coupled dislocation shearing of γ' precipitates in Ni-base superalloys*, Acta Mater. 59 (2011), pp. 3484–3497, Available at http://www.sciencedirect.com/science/article/pii/S1359645411001169.

[21] J.R. Mianroodi, A. Hunter, I.J. Beyerlein, and B. Svendsen, *Theoretical and computational comparison of models for dislocation dissociation and stacking fault/core formation in fcc crystals*, J. Mech. Phys. Solids 95 (2016), pp. 719–741, Available at http://www.sciencedirect.com/science/article/pii/S0022509616300369.

[22] A.G. Khachaturyan, *Theory of Structural Transformations in Solids*, 2008th ed., Dover Publications, Mineola, N.Y, 2008 May.

[23] Y. Wang and J. Li, *Phase field modeling of defects and deformation*, Acta Mater. 58 (2010), pp. 1212–1235, Available at http://www.sciencedirect.com/science/article/pii/S1359645409007447.

[24] T. Mura, *Micromechanics of Defects in Solids*, 2nd ed., Springer, Dordrecht, Netherlands ; Boston : Hingham, MA, USA, 1987 Nov.

[25] V. Bulatov and W. Cai, *Computer simulations of dislocations*, Oxford University Press, Oxford ; New York, 2006 Dec.

[26] C. Shen and Y. Wang, *Phase field model of dislocation networks*, Acta Mater. 51 (2003), pp. 2595–2610, Available at http://www.sciencedirect.com/science/article/pii/S1359645403000582.

[27] G. Schoeck, *The generalized Peierls-Nabarro model*, Philos. Mag. A 69 (1994), pp. 1085–1095, Available at https://doi.org/10.1080/01418619408242240.

[28] G. Grochola, S.P. Russo, and I.K. Snook, *On fitting a gold embedded atom method potential using the force matching method*, J. Chem. Phys. 123 (2005), p. 204719, Available at http://aip.scitation.org/doi/10.1063/1.2124667.

[29] Y. Mishin, D. Farkas, M.J. Mehl, and D.A. Papaconstantopoulos, *Interatomic potentials for monoatomic metals from experimental data and ab initio calculations*, Phys. Rev. B 59 (1999), pp. 3393–3407, Available at http://link.aps.org/doi/10.1103/PhysRevB.59.3393.

[30] A. Hunter, R.F. Zhang, and I.J. Beyerlein, *The core structure of dislocations and their relationship to the material γ-surface*, J. Appl. Phys. 115 (2014), p. 134314, Available at http://aip.scitation.org/doi/10.1063/1.4870462.

[31] F. Willot, *Fourier-based schemes for computing the mechanical response of composites with accurate local fields*, Comptes Rendus Mécanique 343 (2015), pp. 232–245, Available at http://www.sciencedirect.com/science/article/pii/S1631072114002149.

[32] G. Schoeck, *The core structure, recombination energy and Peierls energy for dislocations in Al*, Philos. Mag. A 81 (2001), pp. 1161–1176, Available at https://doi.org/10.1080/01418610108214434.

[33] B.A. Szajewski, A. Hunter, and D.J. Luscher, *Analytic model of the γ-surface deviation and influence on the stacking fault width between partial dislocations*, Comput. Mater. Sci. 147 (2018), pp. 243–250, Available at http://www.sciencedirect.com/science/article/pii/S0927025618301046.

[34] X.Z. Wu, R. Wang, S.F. Wang, and Q.Y. Wei, *Ab initio calculations of generalized-stacking-fault energy surfaces and surface energies for FCC metals*, Appl. Surf. Sci.

256 (2010), pp. 6345–6349, Available at http://www.sciencedirect.com/science/article/pii/S0169433210005106.
[35] Y.M. Juan and E. Kaxiras, *Generalized stacking fault energy surfaces and dislocation properties of silicon: A first-principles theoretical study*, Philos. Mag. 74 (1996), pp. 1367–1384, Available at https://doi.org/10.1080/01418619608240729.
[36] V.A. Vorontsov, C. Shen, Y. Wang, D. Dye, and C.M.F. Rae, *Shearing of γ' precipitates by a $\langle 112 \rangle$ dislocation ribbons in Ni-base superalloys: A phase field approach*, Acta Mater. 58 (2010), pp. 4110–4119, Available at http://www.sciencedirect.com/science/article/pii/S1359645410001990.
[37] V.A. Vorontsov, R.E. Voskoboinikov, and C.M.F. Rae, *Shearing of γ' precipitates in Ni-base superalloys: a phase field study incorporating the effective γ-surface*, Philos. Mag. 92 (2012), pp. 608–634, Available at https://doi.org/10.1080/14786435.2011.630691.
[38] C. Shen and Y. Wang, *Incorporation of γ-surface to phase field model of dislocations: simulating dislocation dissociation in fcc crystals*, Acta Mater. 52 (2004), pp. 683–691, Available at http://www.sciencedirect.com/science/article/pii/S1359645403006207.
[39] S. Zheng, Y. Ni, and L. He, *Phase field modeling of a glide dislocation transmission across a coherent sliding interface*, Modelling Simul. Mater. Sci. Eng. 23 (2015), p. 035002, Available at http://stacks.iop.org/0965-0393/23/i=3/a=035002.
[40] S. Plimpton, *Fast parallel algorithms for short-range molecular dynamics*, J. Comput. Phys. 117 (1995), pp. 1–19, Available at http://www.sciencedirect.com/science/article/pii/S002199918571039X.
[41] E. Bitzek, P. Koskinen, F. Gähler, M. Moseler, and P. Gumbsch, *Structural relaxation made simple*, Phys. Rev. Lett. 97 (2006), p. 170201, Available at http://link.aps.org/doi/10.1103/PhysRevLett.97.170201.
[42] R. Peierls, *The size of a dislocation*, Proc. Phys. Soc. 52 (1940), p. 34, Available at http://stacks.iop.org/0959-5309/52/i=1/a=305.
[43] F.R.N. Nabarro, *Dislocations in a simple cubic lattice*, Proc. Phys. Soc. 59 (1947), p. 256, Available at http://stacks.iop.org/0959-5309/59/i=2/a=309.
[44] B.E. Warren, *X-ray measurement of stacking fault widths in fcc metals*, J. Appl. Phys. 32 (1961), pp. 2428–2431, Available at https://aip.scitation.org/doi/10.1063/1.1777086.
[45] P.C.J. Gallagher, *An absolute determination of the extrinsic and intrinsic stacking fault energies in Ag-In Alloys*, Phys. Stat. Sol. (b) 16 (1966), pp. 95–115, Available at https://onlinelibrary.wiley.com/doi/abs/10.1002/pssb.19660160109.
[46] H. Föll and C.B. Carter, *Direct TEM determination of intrinsic and extrinsic stacking fault energies of silicon*, Philos. Mag. A 40 (1979), pp. 497–510, Available at https://doi.org/10.1080/01418617908234855.
[47] J.D. Eshelby, *LXXXII. Edge dislocations in anisotropic materials*, Philos. Mag. 40 (1949), pp. 903–912, Available at https://doi.org/10.1080/14786444908561420.
[48] F. Kroupa and L. Lejček, *Splitting of dislocations in the Peierls-Nabarro model*, Czech. J. Phys. B 22 (1972), pp. 813–825, Available at https://link.springer.com/article/10.1007/BF01694859.
[49] Z.P. Pi, Q.H. Fang, C. Jiang, B. Liu, Y. Liu, P.H. Wen, and Y.W. Liu, *Stress dependence of the dislocation core structure and loop nucleation for face-centered-cubic metals*, Acta Mater. 131 (2017), pp. 380–390, Available at http://www.sciencedirect.com/science/article/pii/S1359645417303014.
[50] S.I. Ranganathan and M. Ostoja-Starzewski, *Universal elastic anisotropy index*, Phys. Rev. Lett. 101 (2008), p. 055504, Available at http://link.aps.org/doi/10.1103/PhysRevLett.101.055504.
[51] B.A. Szajewski, A. Hunter, D.J. Luscher, and I.J. Beyerlein, *The influence of anisotropy on the core structure of Shockley partial dislocations within FCC materials*, Modelling Simul. Mater. Sci. Eng. 26 (2018), p. 015010, Available at http://stacks.iop.org/0965-0393/26/i=1/a=015010.
[52] J.W. Cahn and J.E. Hilliard, *Free energy of a nonuniform system. I. Interfacial free*

energy, J. Chem. Phys. 28 (1958), pp. 258–267, Available at https://aip.scitation.org/doi/abs/10.1063/1.1744102.